Journal of Materials Chemistry A

ROYAL SOCIETY OF CHEMISTRY

PAPER

View Article Online
View Journal | View Issue



Check for updates

Cite this: *J. Mater. Chem. A*, 2024, **12**, 14419

# Fluorosulfide $La_{2.7}Ba_{6.3}F_{8.7}S_6$ with a double-layer honeycomb structure enabling fluoride-ion conduction†

Shintaro Tachibana, [a] Chengchao Zhong, *[a] Takeshi Tojigamori, [b] Hidenori Miki, [b] Toshiyuki Matsunaga[c] and Yuki Orikasa *[a]

Received 12th December 2023
Accepted 7th April 2024

DOI: 10.1039/d3ta07680f

rsc.li/materials-a

Mixed-anion compounds comprise anion-ordered layered structures with fluoride-ion conducting layers, which are not found in conventional metal fluorides. Hence, they represent a new frontier in the search for fluoride-ion conductors. Previous studies investigated only mixed-anion compounds with known crystal structures, but failed to exploit a flexible structural design. In this study, we performed a materials search based on the ternary phase diagram of $BaS–LaF_3–BaF_2$ for new fluorosulfide phases and found an unreported fluorosulfide, $La_{2.7}Ba_{6.3}F_{8.7}S_6$, showing a fluoride-ion conductivity of $4.23 \times 10^{-7}$ S cm$^{-1}$ at 343 K. $La_{2.7}Ba_{6.3}F_{8.7}S_6$ forms an anion-ordered two-dimensional crystal lattice with double-honeycomb $(La–Ba)F_2$ fluoride-ion-conducting layers, which cannot be realized in single-anion compounds. In the $(La–Ba)F_2$ layers, the fluoride-ion conduction is realized through normal F1 site and interstitial F2 site *via* a vacancy mechanism. The presence of sulfide ions in the crystal structure contributes to the spreading of $(La–Ba)F_2$ layers along the *ab* plane, resulting in a longer La–F distance. Material development using a systematic phase diagram search on fluorosulfides allows to increase the variation of the crystal structure for fluoride-ion conductors and to discover the novel fluoride-ion conducting layers that are inaccessible to single anion compounds.

## Introduction

Mixed-anion compounds containing more than one anionic species are driving the exploration of solid-state materials with novel properties.[1–3] Anions with different ionic radii, polarizabilities, and electronegativities prefer different coordination environments and exist in different layers of their crystal structures. Therefore, mixed-anion compounds can be used to create novel crystal structures with functional layers that are inaccessible to single-anion compounds. For example, the FeAs layer of REFeAsO (RE = rare earth metal) induces superconductivity when it is electron-doped by fluorine substitution in the adjacent LaO layer. In the thermoelectric materials of layered $Sr_2MCu_2Te_2O_2$ (M = Mn, Co, and Zn), an antifluorite $Cu_2Te_2$ layer with a large anionic radius is the path for charge transport and provides an excellent Seebeck effect.[4] In layered oxyhalide compounds, the electronic structure and band gap can be optimized by controlling the thickness and stacking pattern of the fluorite layers, resulting in stable visible-light water-splitting reactions.[5–7]

A fluoride ion is monovalent and has a small ionic radius, similar to lithium and sodium ions; therefore, the fluoride ion is a highly conductive carrier expected to be applicable in solid electrolytes of solid-state batteries.[8] The fluoride-ion conductors that have been studied thus far are mainly single-anion compounds whose crystal structures have been mostly restricted to three types:[9,10] fluorite-type [$MSnF_4$ (ref. 11) (M = Pb, Ba), $Ba_{0.6}La_{0.4}F_{2.4}$],[12] tysonite-type [$La_{0.9}Ba_{0.1}F_{2.9}$],[13] and perovskite-type [$CsPb_{0.95}K_{0.05}F_{2.95}$].[14] In comparison, fluoride-ion conductors with mixed anions, such as oxyfluoride and fluorosulfide, exhibit conduction paths that are not found in conventional fluorides. Among oxyfluorides, $Bi_{0.8}Pb_{0.2}O_{0.8}F_{1.2}$, $LaO_{0.6}F_{1.8}$, and $La_{0.8}Mg_{0.2}O_{0.9}F$ with PbFCl-type structures have been reported as fluoride-ion conductors in which the fluoride ion conducts in a double fluoride-ion layer.[15–17] We previously synthesized the fluorosulfide $La_{2+x}Sr_{1-x}F_{4+x}S_2$ ($-0.1 \leq x \leq 0.2$) with PbFCl-type (La–Sr)FS and fluorite-type $(La–Sr)F_2$ crystal structures in a ratio of 1 : 2, resulting in two-dimensional fluoride-ion conduction in the triple-fluorite layers.[18] However, studies on fluoride-ion conduction in mixed-anion compounds are limited to the reported crystal structures. Recently, Kato *et al.* studied the La–F–X (X = Cl, Br, and I) ternary phase using an evolutionary algorithm and found that the new phase $LaF_2I$

[a]*Graduate School of Life Sciences, Ritsumeikan University, 1-1-1 Noji-higashi, Kusatsu, Shiga 525-8577, Japan. E-mail: zhong@fc.ritsumei.ac.jp; orikasa@fc.ritsumei.ac.jp*

[b]*Advanced Material Engineering Division, Toyota Motor Corporation, 1200 Mishuku, Susono, Shizuoka 410-1193, Japan*

[c]*Graduate School of Human and Environmental Studies, Kyoto University, Yoshida-nihonmatsu-cho, Sakyo, Kyoto 606-8501, Japan*

† Electronic supplementary information (ESI) available. See DOI: https://doi.org/10.1039/d3ta07680f

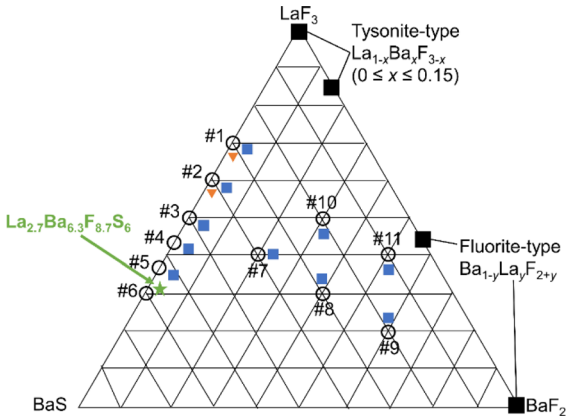


Fig. 1 Pseudo-ternary phase diagram of the BaS–$LaF_3$–$BaF_2$ system. The numbers #1 to #11 indicate the synthesized phases. Blue squares and orange triangles indicate the areas where $Ba_2LaF_7$ and LaFS are present, respectively.

exhibits fluoride-ion conductivity.[19] Thus, the undiscovered crystal structure of mixed-anion compounds could be a new platform for fluoride-ion conductors.

In this study, we explore the pseudo-ternary systems of BaS–$LaF_3$–$BaF_2$ (Fig. 1) by systematic material synthesis through solid-state reactions. We discovered a new phase $La_{2.7}Ba_{6.3}F_{8.7}S_6$, with an alternative stacking of (La–Ba)$S_2$ layers and (La–Ba)$F_2$ layers. In the (La–Ba)$F_2$ layer, the cations and anions form a honeycomb lattice, with an interstitial fluoride-ion site at the center of the double-layer honeycomb, forming a two-dimensional fluoride-ion conduction pathway. $Ca^{2+}$ and fluoride vacancies can be introduced into the crystal structure to form $La_{2.7-x}Ba_{6.3-x}Ca_xF_{8.7-x}S_6$ ($0 \leq x \leq 0.54$), resulting in increased fluoride-ion conductivity. Based on crystal structure analysis, the presence of sulfide ions in fluorosulfides contributes to expanding the (La–Ba)$F_2$ layers and forming the novel double-layer honeycomb structure that allows the migration of fluoride ions.

## Experimental terms

To explore the BaS–$LaF_3$–$BaF_2$ ternary phase system, BaS (Kojundo Chemical Industries, Ltd., 99.9%), $LaF_3$ (Sigma-Aldrich, 99.99%) and $BaF_2$ (Wako Pure Chemical Industries, Ltd., 99.9%) were weighted in a different molar ratio. For $Ca^{2+}$-substituted $La_{2.7-x}Ba_{6.3}Ca_xF_{8.7-x}S_6$ ($x = 0$, 0.27, 0.54) compounds, La metal (Sigma-Aldrich, 99.9%), $LaF_3$ (Sigma-Aldrich, 99.99%), $BaF_2$ (Wako Pure Chemical Industries, Ltd., 99.9%), BaS (Kojundo Chemical Industries, Ltd., 99.9%), S powder (Wako Pure Chemical Industries, Ltd., 98.0%) and $CaF_2$ (Wako Pure Chemical Industries, Ltd. 99.9%) were weighed in a stoichiometric ratio. Samples were mixed using a mortar under an argon atmosphere and compressed into $\varphi$ 10 pellets. The pellet sample was placed in a tantalum container and vacuum-sealed in a quartz tube. Samples were calcined at 1223 K for 48 h with an intermediate grinding.

The crystal structure of the synthesized compounds was analyzed by X-ray diffraction (XRD) and neutron diffraction (ND). XRD measurements were carried out at the beamline BL5S2 of Aichi SR. The measurements were performed with a Debye–Scherrer optical system at a wavelength of 0.7504 Å using a PILATUS detector. The samples were thoroughly ground to uniform particles and poured into a Lindemann glass capillary with a diameter of 0.3 mm in air. The La/Ba ratio was determined by inductively coupled plasma atomic emission spectroscopy (ICP-AES). The chemical composition of sulfur and fluorine was examined by infrared absorption spectroscopy and ion chromatography, respectively.

The crystal structure of the synthesized compounds was solved from powder diffraction data by direct-space methods and was refined by the Rietveld refinement (Fig. S1†). The unit-cell parameters were indexed using 20 reflections in the XRD data and the autoindexing program DICVOL06 integrated in Match-3 software (Crystal Impact GbR, Bonn, Germany), and the validity of the space group was determined by subsequent structural analysis. The initial structure of the synthesized compounds was achieved by the direct-space method using the ENDEAVOUR software (Crystal Impact GbR, Bonn, Germany), consists of a combined global optimization of the difference between experimental and calculated diffraction data and the potential energy of the system.[20] The structural parameters of initial structure were refined by Rietveld refinement within the JANA2006 software. The validity of the refined structure model was evaluated by the oxidation states of the individual sites calculated using the bond valence sums (BVS).

ND measurements were performed using the iMATERIA located in the beamline BL20 of the Materials and Life Science Experimental Facility, Japan Proton Accelerator Research Complex (J-PARC MLF). The diffracted neutrons were detected using $^3$He gas-filled one-dimensional position-sensitive neutron detectors installed in backward, 90° and low-angle banks. The synthesized samples were ground uniformly, and then poured into a cylindrical vanadium–nickel-alloy holder with a diameter of 6 mm and thickness of 0.1 mm and sealed in air. Diffraction intensities for the time-of-flight were collected at 298 K in argon atmosphere. The Rietveld refinement and maximum entropy method (MEM) were performed using the crystal structure analysis software Z-Rietveld using the diffraction pattern of the backward bank.[21,22] The bond-valence-based energy landscapes (BVELs) for fluoride ions were calculated using soft-BV,[23] where the spatial resolution was set at 0.1 Å. The three-dimensional nuclear density distribution was determined using the VESTA program.[24]

Alternative current (AC) impedance was performed in air using HZ-7000 (Hokuto Denko) to evaluate the ionic conductivity of the synthesized compounds. The synthesized compounds were formed into pellets with a diameter of 10 mm by cold isostatic pressing at 190 MPa. The pelletized samples were sintered at 1223 K for 24 hours under vacuum. The sintered pellets were sputtered with gold on both sides under vacuum and placed in a 10 mm diameter cylindrical cell with a stainless steel (SS) current collector. The measurements were performed in the frequency range of 500 kHz to 0.1 Hz at an amplitude of 100 mV, under the temperature range of 343 K to 423 K in steps of 10 K.

 

In order to confirm the dominant carrier species of the $La_{2.7}Ba_{6.3}F_{8.7}S_6$ compounds, AC impedance and two-probe direct current (DC) conductivity measurements were performed in air using a symmetric SS|Pb|$PbSnF_4$|$La_{2.7}Ba_{6.3}F_{8.7}S_6$-|$PbSnF_4$|Pb|SS cell with a HZ-7000 potentiostat under 423 K. AC impedance were measured in the frequency range from 500 kHz to 0.1 Hz with an amplitude of 100 mV. For the DC method, the current was applied for 10 s at 0.2 μA intervals from 1.0 μA to 2.2 μA, and relaxation was performed for 70 s. The slope of *I*–*V* plots using the data obtained for current and voltage at 2 s was used as the resistance value.

Cyclic voltammetry was performed in air using a HZ-7000 potentiostat to evaluate the electrochemical potential window. A SS|Pt|$La_{2.7}Ba_{6.3}F_{8.7}S_6$|Pb/$PbF_2$|SS cell was fabricated in a 10 mm diameter cylindrical cell with a metal plate, electrolyte, and composite electrode. The composite electrode was prepared by mixing Pb and $PbF_2$ powders at a ratio of 1 : 1. The voltage scanning range was from −5.0 to 5.0 V with a scanning speed of 0.2 mV $s^{-1}$ under 423 K.

## Results and discussion

The binary systems between $LaF_3$ and $BaF_2$ have been extensively studied, in which tysonite-type $La_{1-x}Ba_xF_{3-x}$ ($0 \leq x \leq 0.15$) and fluorite-type $Ba_{1-y}La_yF_{2+y}$ have already been reported as fluoride-ion conductors.[12,13,25–27] We extended this binary system to the BaS–$LaF_3$–$BaF_2$ ternary phase system (Fig. 1) for exploring new fluorosulfides. Synthesis using $LaF_3$, $BaF_2$, and BaS (#7–#11 in Fig. 1) yields $Ba_2LaF_7$ fluorides with a small amount of an unknown sulfide-based phase. In the $LaF_3$–BaS system, when the composition ratio becomes BaS : $LaF_3$ = 30 : 70, fluorosulfide LaFS appears (#1). On the other hand, the amount of $Ba_2LaF_7$ decreases with increasing BaS composition ratio (#2–#5). Synthesis using the molar ratio BaS : $LaF_3$ = 70 : 30 (green star in Fig. 1) did not yield $Ba_2LaF_7$, the starting material, or previously reported fluorosulfides as impurities (Fig. S2 and S3a†), indicating that unreported compound was obtained.

The X-ray diffraction (XRD) pattern of the synthesized phase was indexed to a hexagonal phase $R\bar{3}$ (148) space group, with lattice parameters of $a = 4.3862(11)$ Å and $c = 32.418(13)$ Å. The crystal structure of the synthesized sample was determined using a combination of the direct-space method and Rietveld analysis ($R_{wp} = 11.01\%$, $R_p = 6.23\%$ and $S = 1.19$). The obtained chemical composition of the structure is $La_3Ba_6F_9S_6$, which is slightly different from the preparation ratio of the starting materials (La : Ba : F : S = 3 : 7 : 9 : 7). The discrepancy in compositional ratios is due to the presence of unknown impurities, as suggested by the X-ray diffraction patterns at $2\theta = 13.0°$ and 16.7° that cannot be indexed by $La_3Ba_6F_9S_6$ (Fig. S3c†). In order to remove impurities, the synthesis was attempted using different ratios of starting materials, but the raw material ratio of La : Ba : F : S = 3 : 7 : 9 : 7 was the best condition with the fewest impurities.

$La_3Ba_6F_9S_6$ has a cation-ordered structure comprised one lanthanum site (3b), one barium site (6c), and three anion sites (6c, 6c, and 3a). The bond valence sum was +2.03 for the lanthanum site and +2.33 for the barium site, suggesting that the sites were mixed. Furthermore, elemental analysis using ICP-AES, infrared absorption spectroscopy, and ion chromatography of the synthesized phase revealed a chemical composition of La : Ba : F : S = 2.7 : 6.3 : 8.4 : 6.1. Therefore, we performed an additional Rietveld analysis using these three constraints: (i) random occupation of the cation sites by lanthanum and barium; (ii) application of the elemental analysis result of La/Ba = 2.7/6.3; and (iii) introduction of vacancies in the anion sites owing to the decrease in the total charge of the cations. The structural refinement converged smoothly ($R_{wp}$ = 10.98%, $R_p$ = 6.19%, and $S$ = 1.18), indicating that Rietveld refinement was more reliable (Fig. S3c and Table S2†). Subsequently, we performed neutron diffraction (ND) analysis to refine the site parameters of the fluoride ions. The Rietveld profile of the ND pattern of $La_{2.7}Ba_{6.3}F_{8.7}S_6$ is shown in Fig. 2a; the reliability factors $R_{wp}$, $R_e$, and $S$ are 8.84%, 1.41%, and 6.25, respectively. The refined structural parameters of $La_{2.7}Ba_{6.3}F_{8.7}S_6$ are listed in Table S3.†

$La_{2.7}Ba_{6.3}F_{8.7}S_6$ has a two-dimensional layered crystal structure, with two (La–Ba)$S_2$ layer sandwiched by a (La–Ba)$F_2$ layer (Fig. 2b and S3d†). The fluoride- and sulfide-ion layers spanning the *ab* plane are present across the cation layers, which is attributed to the difference in anionic size.[28,29] The unit cell has two cation sites 3b and 6c: the 3b site (upper right in Fig. S3d†) is isotopically coordinated to six sulfide ions (site occupancy $La^{3+}$ : $Ba^{2+}$ = 0.457(2) : 0.543(2)), whereas the 6c site (lower right in Fig. S3d†) is anisotropic, coordinating to seven fluoride ions and three sulfide ions (site occupancy $La^{3+}$ : $Ba^{2+}$ = 0.2216(10) : 0.7784(10)). Sulfide ions occupy the 6c sites, which are coordinated to three La1 and three La2 sites.

$La_{2.7}Ba_{6.3}F_{8.7}S_6$ has two fluoride-ion sites 6c and 3a in the (La–Ba)$F_2$ layers. The 6c site (upper right of Fig. 2b) is a tetrahedral site coordinated to four La2 sites, and the 3a site (lower right of Fig. 2b) is an octahedral site coordinated to six La2 sites. The La2–F1 bonds are anisotropic, forming three short La2–F1 bonds (2.60 Å) and one long La2–F1 bond (2.70 Å), whereas the La2–F2 bond lengths are identical (3.02 Å). The La2–F1 distances are comparable to the Ba–F bond lengths in the fluorite-type structure $BaF_2$ (2.68 Å) and the La–F bond lengths in the fluorosulfide LaFS (2.58 Å).[30,31] The La2–F2 distances are longer than those of the previously reported fluorides. The (La–Ba)$S_2$ layers containing sulfide ions with higher polarizability spread in the *ab* plane, inducing the spread of the (La–Ba)$F_2$ layers, and ultimately resulting in a longer La–F distance.

The (La–Ba)$F_2$ layers have a honeycomb structure of cations and anions when observed from the *c*-axis (Fig. 2c). The honeycomb structure has attracted attention in physics owing to its magnetic properties, particularly in research areas pertaining to superconductors and semiconductors.[32] In fluoride-ion conductors, the only reported double-layer honeycomb structure is $LaF_2I$, with a triangular fluoride-ion site in the honeycomb framework and another tetrahedral fluoride-ion site between the two honeycomb-structured layers. The double-layer honeycomb structure of $La_{2.7}Ba_{6.3}F_{8.7}S_6$ is different from that of $LaF_2I$, with an octahedral site between two layers (*vs.* tetrahedral site in $LaF_2I$, Fig. S4†), which is identical to the

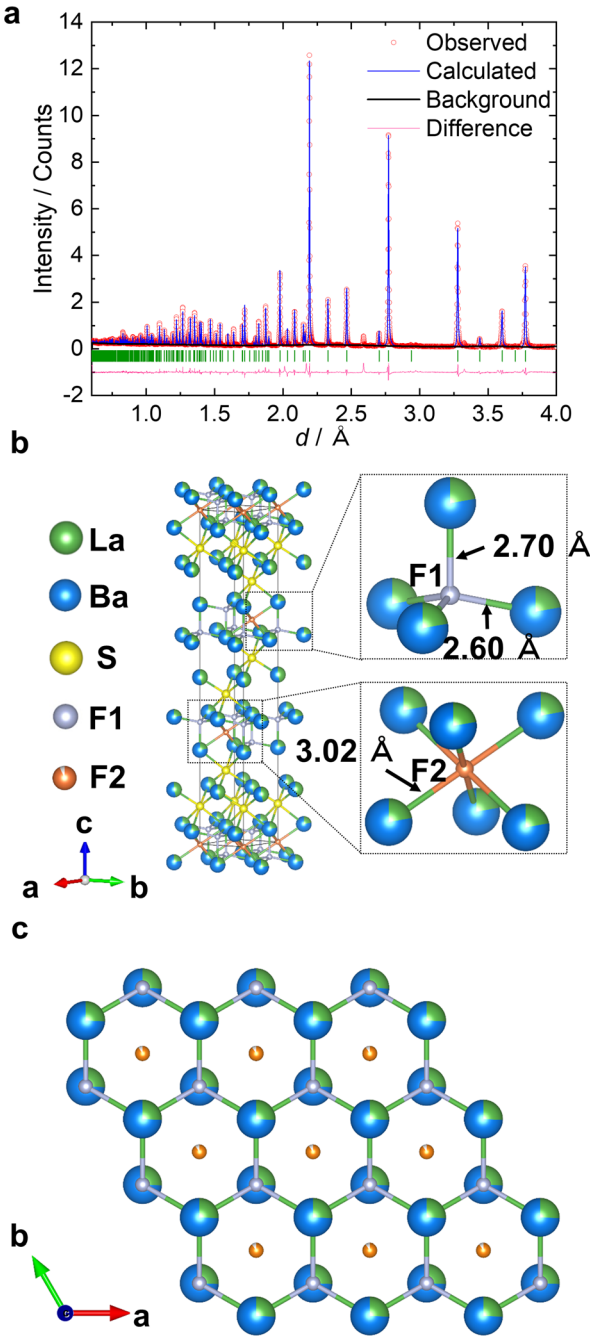


Fig. 2 Structural characterization of $La_{2.7}Ba_{6.3}F_{8.7}S_6$ by neutron diffraction. (a) Neutron diffraction profile for the Rietveld refinement of $La_{2.7}Ba_{6.3}F_{8.7}S_6$. Green ticks represent the Bragg position of $La_{2.7}Ba_{6.3}F_{8.7}S_6$. (b) Refined crystal structure of $La_{2.7}Ba_{6.3}F_{8.7}S_6$ (space group: $R\bar{3}$). The unit cell is shown by solid lines. Two fluoride-ion sites exist: the normal F1 site and the interstitial F2 site. (c) Enlarged view of the crystal structure of $La_{2.7}Ba_{6.3}F_{8.7}S_6$ along the *ab* plane.

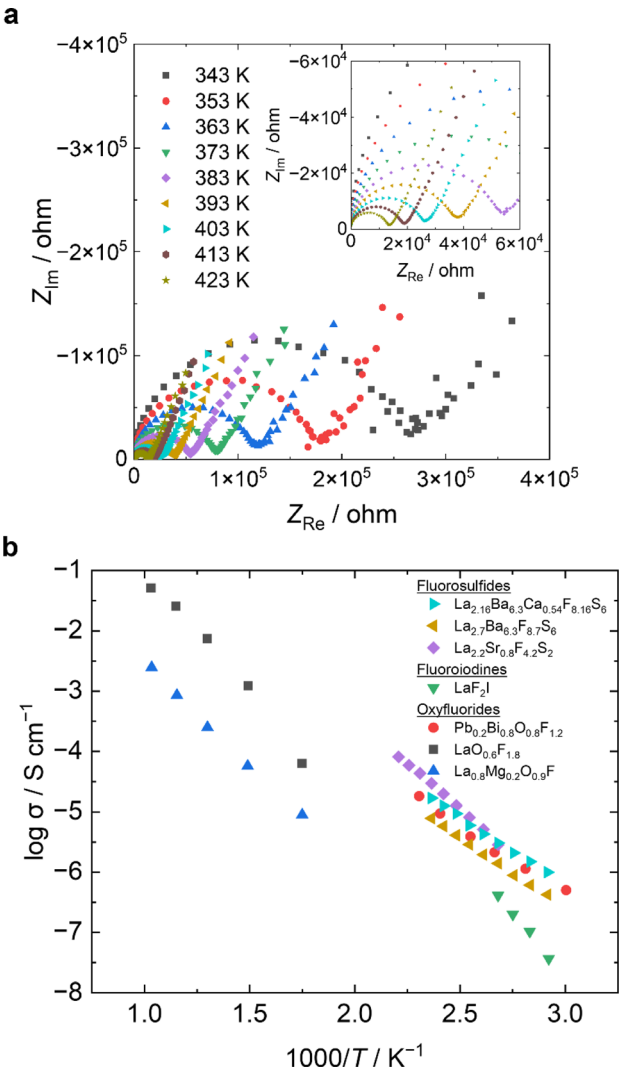


Fig. 3 Electrochemical properties of $La_{2.7}Ba_{6.3}F_{8.7}S_6$. (a) Nyquist plots of the SS|$La_{2.7}Ba_{6.3}F_{8.7}S_6$|SS cell at each temperature. A symmetric cell was used to conduct AC impedance between 343 K and 423 K at an amplitude of 100 mV and a frequency of 500 kHz to 0.1 Hz. (b) Arrhenius plots of the fluoride-ion conductivity for the mixed-anion compounds.

$Ba_2H_3$ slab in $Ba_2H_3X$ (X = Cl, Br, I) that shows the highest $H^-$ conductivity at 300 K.[33]

Fig. 3a shows the Nyquist plots of the synthesized $La_{2.7}Ba_{6.3}F_{8.7}S_6$ compounds based on their AC impedance profiles. The plots show a distorted semicircle at high frequencies and a straight line at low frequencies, which is similar to the Nyquist plots of previously reported fluoride-ion conductors.[12,34,35] In the Nyquist plots of ion conductors, the diameter of the semicircle at high frequency side corresponds to the electrolyte resistance and the straight line on the low frequency side is related to the polarization phenomenon at the electrode/electrolyte interface (Fig. S5a and b).† Fig. 3b shows the Arrhenius plots of log $\sigma$ *vs.* $1000/T$ for the mixed-anion compounds,[16–19] where $\sigma$ is the conductivity measured by AC impedance. $La_{2.7}Ba_{6.3}F_{8.7}S_6$ exhibits a fluoride-ion conductivity of $4.23 \times 10^{-7}$ S cm$^{-1}$ at 343 K, which is several orders of magnitude higher than that of other mixed-anion compounds, such as fluoroiodines ($LaF_2I$) and oxyfluorides ($LaO_{0.6}F_{1.8}$).[17,19] The activation energy for $La_{2.7}Ba_{6.3}F_{8.7}S_6$ is 0.50 eV, which is lower than those of $La_{2.2}Sr_{0.8}F_{4.2}S_2$ (0.64 eV), $LaF_2I$ (0.87 eV), and $LaO_{0.6}F_{1.8}$ (0.62 eV).[17–19] Hence, the $La_{2.7}Ba_{6.3}F_{8.7}S_6$ phase exhibits the lowest activation energy among previously reported mixed-anion compounds.

To clarify the dominant carrier species of the $La_{2.7}Ba_{6.3}F_{8.7}S_6$ compounds, two-probe direct current (DC) method were performed using a SS|Pb|$PbSnF_4$|$La_{2.7}Ba_{6.3}F_{8.7}S_6$|$PbSnF_4$|Pb|SS symmetrical blocking cell (Fig. S5c†). Since $PbSnF_4$ is an almost pure fluoride-ion conductor, only fluoride ions are allowed to conduct under DC method. The cell consists of the electrolyte ($La_{2.7}Ba_{6.3}F_{8.7}S_6$ and $PbSnF_4$) resistance component, the interphase electrolyte resistance ($La_{2.7}Ba_{6.3}F_{8.7}S_6$/$PbSnF_4$), and the resistive interphases by the decomposition of $PbSnF_4$ at the $PbSnF_4$/Pb interface (Fig. S5d†). The resistance values observed in the DC impedance measurements are similar to those obtained by the AC method in this symmetric blocking cell, despite the resistance from the decomposition of $PbSnF_4$ (Fig. S6†). Hence, the fluoride ions are the conduction carriers of $La_{2.7}Ba_{6.3}F_{8.7}S_6$.[35]

Introducing the fluoride-ion vacancies is an effective way to further improve the ionic conductivity. Since divalent calcium ions (100 pm) and trivalent lanthanum ions (103 pm) have nearly the same ionic radius, lanthanum ions can be replaced by calcium ions, which is expected to result in vacancies for fluoride ions. The variation in the lattice parameters of the synthesized $La_{2.7-x}Ba_{6.3-x}Ca_xF_{8.7-x}S_6$ ($x = 0.27, 0.54$) according to Vegard's law indicates that divalent $Ca^{2+}$ ions can be substituted into trivalent $La^{3+}$ ions in this crystal structure (Fig. S7a and b†). $La_{2.16}Ba_{6.3}Ca_{0.54}F_{8.16}S_6$ shows the highest fluoride-ion conductivity ($9.97 \times 10^{-7}$ S cm$^{-1}$) at 343 K, which is twice that of $La_{2.7}Ba_{6.3}F_{8.7}S_6$ (Fig. S7c†). The structural parameters of $La_{2.16}Ba_{6.3}Ca_{0.54}F_{8.16}S_6$, refined by the Rietveld analysis of the ND patterns, indicating that the variation in the fluoride-ion conductivity arises from the increase in fluoride-ion vacancies (Fig. S7d and Table S4†). The cyclic voltammogram of the SS|Pb/$PbF_2$|$La_{2.7}Ba_{6.3}F_{8.7}S_6$|Pt|SS cells indicates that $La_{2.7}Ba_{6.3}F_{8.7}S_6$ compounds exhibit a wide electrochemical potential window (Fig. S8†). Cathodic currents are observed below −2.0 V, whereas anodic currents are observed above 2.0 V. Therefore, the electrochemical potential window of $La_{2.7}Ba_{6.3}F_{8.7}S_6$ is −2.0 V to 2.0 V *vs.* Pb/$PbF_2$, which is wider than that of $La_{2.2}Sr_{0.8}F_{4.2}S_2$ and comparable to the oxidation potential window of $La_{0.9}Ba_{0.1}F_{2.9}$.[18]

$La_{2.7}Ba_{6.3}F_{8.7}S_6$ has a (La–Ba)$F_2$ layer with a honeycomb structure spanning the *ab* plane (Fig. 4). Six adjacent F1 sites were observed around the interstitial F2 sites. The F1–F2 distance was 2.74 Å, which is the shortest among other distances such as those of F1–F1 (3.31 Å) and F2–F2 (4.39 Å). Therefore, the expected fluoride-ion conduction path is ⋯F1–F2–F1⋯, as shown by the black dotted arrows in Fig. 4, indicating a two-dimensional fluoride-ion conduction pathway. The occupancies of the F1 and F2 sites in $La_{2.7}Ba_{6.3}F_{8.7}S_6$ were 0.9859(7) and 0.9281(14), respectively, indicating that fluoride-ion conduction could have occurred *via* the vacancy mechanism. This is evidenced by an improved conductivity in the $Ca^{2+}$-substituted material along with an increase in defects (Fig. 3b). The nuclear density distribution of $La_{2.7}Ba_{6.3}F_{8.7}S_6$ obtained from the maximum entropy method revealed that the fluorine density was distributed from interstitial F2 sites to normal F1 sites (Fig. S9†). Furthermore, the bond-valence-based energy landscapes (BVELs) of $La_{2.7}Ba_{6.3}F_{8.7}S_6$ (Fig. S10†) indicate that the fluoride ion migrates from the normal F1 sites to the interstitial F2 sites, allowing two-dimensional fluoride-ion conduction. Hence, the crystal structure of $La_{2.7}Ba_{6.3}F_{8.7}S_6$ has a two-dimensional fluoride-ion conduction pathway in the double-honeycomb (La–Ba)$F_2$ layers *via* a vacancy mechanism between the normal F1 site and the interstitial F2 site.

The (La–Ba)$F_2$ layers are similar to the fluoride-ion conduction layers of $LaF_2I$ and $La_{0.9}Ba_{0.1}F_{2.9}$ with a honeycomb structure along the *ab* plane (Fig. S4†). The $LaF_2I$ crystal structure contains two fluoride-ion sites—a tetrahedral F1 site and a triangle F2 site, while the $La_{0.9}Ba_{0.1}F_{2.9}$ crystal structure contains three fluoride-ion sites—a tetrahedral F1 site and two triangle sites (F2 and F3). In comparison, $F^-$ in $La_{2.7}Ba_{6.3}F_{8.7}S_6$ conducts using the double-layer honeycomb lattice with tetrahedral F1 sites and octahedral F2 sites. The different coordination environment of fluoride-ion sites in $La_{2.7}Ba_{6.3}F_{8.7}S_6$ compared to that of the other compounds indicates that the conduction mechanism of $La_{2.7}Ba_{6.3}F_{8.7}S_6$ is completely new.

The discovery of new functional layers has the potential to accelerate material development. In the field of superconductivity, the discovery of the $CuO_2$-superconducting layer can allow us to surpass the limit of the superconducting transition temperature predicted by past theories, considerably revitalizing this field.[36] Mixed-anion compounds containing anions with different ionic radii are ideal for the development of functional anion layers because they comprise anion-ordered layered structures. Thus far, the development of fluoride-ion conductors has focused on single-anion fluorides with a limited crystal structure; hence, the developed "mixed-anion" strategy could provide a new direction. In this study, a systematic phase diagram search was performed, and an unreported fluorosulfide $La_{2.7}Ba_{6.3}F_{8.7}S_6$ with a new fluoride-ion-conducting double-layer honeycomb structure was found. In the future, by combining the exploration of phase diagrams with theoretical prediction using material informatics, numerous undiscovered mixed-anion compounds with novel fluoride-ion-conducting layers are expected to be found, contributing to the development of solid electrolytes for all-solid-state batteries and gas sensors.

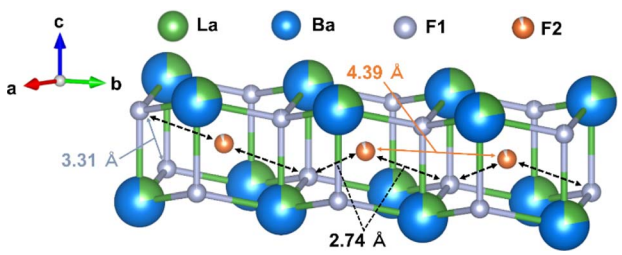


Fig. 4 Enlarged view of the (La–Ba)$F_2$ layer in the $La_{2.7}Ba_{6.3}F_{8.7}S_6$ phase. The gray and orange arrows indicate F1–F2 distances (3.31 Å) and F2–F2 distances (4.39 Å), respectively. Black dotted arrows indicate the direction of the fluoride-ion F1–F2–F1 diffusion pathway.

## Conclusions

In this study, we found a new fluoride-ion conductor $La_{2.7}Ba_{6.3}F_{8.7}S_6$ in the BaS–$LaF_3$–$BaF_2$ ternary system. In

$La_{2.7}Ba_{6.3}F_{8.7}S_6$, the (La–Ba)$F_2$ layer forms a double-layered honeycomb structure and exhibits two-dimensional fluoride-ion conduction through tetrahedral F1 sites and interstitial octahedral F2 sites *via* the vacancy mechanism. The presence of sulfur in the crystal structure led to an expansion of the (La–Ba)$F_2$ layer along the *ab* plane, providing longer La–F bonds. The introduction of additional fluoride-ion vacancies by substituting $La^{3+}$ sites with $Ca^{2+}$ resulted in $La_{2.7-x}Ba_{6.3-x}Ca_xF_{8.7-x}S_6$ ($x$ = 0, 0.27, and 0.54) compounds, which exhibited the highest fluoride-ion conductivity among all previously reported mixed-anion compounds below 343 K. The discovery of new fluoride-ion conductive layers in mixed-anion compounds can bring about a new paradigm shift in the field of fluoride-ion conductors, contributing to the development of all-solid-state fluoride-ion batteries.

## Author contributions

S. T., C. Z., and Y. O. conceived the experiments. S. T., T. T., and H. K. synthesized the materials. Y. O. conducted synchrotron XRD measurements and NPD measurements. S. T. performed electrochemical measurements. S. T. analyzed the electrochemical data. S. T., C. Z., and T. M. carried out the structural analysis. S. T., C. Z., and Y. O. wrote the manuscript. All authors discussed the results and contributed to the final version of the manuscript.

## Conflicts of interest

The authors declare no conflicts of interest associated with this manuscript.

## Acknowledgements

This work was supported by JSPS KAKENHI Grant Numbers JP21J22054, JP19K22239, and JP19H02694. Synchrotron XRD experiments were performed at beamline BL5S2 of Aichi-SR. ND measurements were approved by the Neutron Scattering Program Advisory Committee of the Institute of Material Structure Science, High Energy Accelerator Research Organization (KEK) (proposal no. 2022BM0004). We are grateful to Dr T. Ishigaki in KEK for supporting the ND measurements.

## Notes and references

1 H. Kageyama, K. Hayashi, K. Maeda, J. P. Attfield, Z. Hiroi, J. M. Rondinelli and K. R. Poeppelmeier, *Nat. Commun.*, 2018, **9**, 772.
2 J. K. Harada, N. Charles, K. R. Poeppelmeier and J. M. Rondinelli, *Adv. Mater.*, 2019, **31**, 1805295.
3 K. Maeda, F. Takeiri, G. Kobayashi, S. Matsuishi, H. Ogino, S. Ida, T. Mori, Y. Uchimoto, S. Tanabe, T. Hasegawa, N. Imanaka and H. Kageyama, *Bull. Chem. Soc. Jpn.*, 2022, **95**, 26–37.
4 D. Song, G. Guélou, T. Mori, M. Ochi, K. Kuroki, H. Fujihisa, Y. Gotoh, Y. Iwasa, H. Eisaki and H. Ogino, *J. Mater. Chem. C*, 2018, **6**, 12260–12266.
5 C. Zhong, D. Kato, K. Ogawa, C. Tassel, F. Izumi, H. Suzuki, S. Kawaguchi, T. Saito, A. Saeki, R. Abe and H. Kageyama, *Inorg. Chem.*, 2021, **60**, 15667–15674.
6 A. Nakada, D. Kato, R. Nelson, H. Takahira, M. Yabuuchi, M. Higashi, H. Suzuki, M. Kirsanova, N. Kakudou, C. Tassel, T. Yamamoto, C. M. Brown, R. Dronskowski, A. Saeki, A. Abakumov, H. Kageyama and R. Abe, *J. Am. Chem. Soc.*, 2021, **143**, 2491–2499.
7 D. Kato, O. Tomita, R. Nelson, M. A. Kirsanova, R. Dronskowski, H. Suzuki, C. Zhong, C. Tassel, K. Ishida, Y. Matsuzaki, C. M. Brown, K. Fujita, K. Fujii, M. Yashima, Y. Kobayashi, A. Saeki, I. Oikawa, H. Takamura, R. Abe, H. Kageyama, T. E. Gorelik and A. M. Abakumov, *Adv. Funct. Mater.*, 2022, **32**, 2204112.
8 R. D. Shannon, *Acta Crystallogr., Sect. A: Cryst. Phys., Diffr., Theor. Gen. Crystallogr.*, 1976, **32**, 751–767.
9 L. N. Patro and K. Hariharan, *Solid State Ionics*, 2013, **239**, 41–49.
10 K. Motohashi, T. Nakamura, Y. Kimura, Y. Uchimoto and K. Amezawa, *Solid State Ionics*, 2019, **338**, 113–120.
11 G. Denes, T. Birchall, M. Sayer and M. Bell, *Solid State Ionics*, 1984, **13**, 213–219.
12 C. Rongeat, M. A. Reddy, R. Witter and M. Fichtner, *J. Phys. Chem. C*, 2013, **117**, 4943–4950.
13 C. Rongeat, M. A. Reddy, R. Witter and M. Fichtner, *ACS Appl. Mater. Interfaces*, 2014, **6**, 2103–2110.
14 J. Wang, J. Hao, C. Duan, X. Wang, K. Wang and C. Ma, *Small*, 2022, **18**, e2104508.
15 S. Matar, J. M. Reau, L. Rabardel, G. Demazeau and P. Hagenmuller, *Solid State Ionics*, 1983, **11**, 77–81.
16 M. Momai, S. Tamura, S. Saeki and N. Imanaka, *J. Ceram. Soc. Jpn.*, 2020, **128**, 863–865.
17 M. Momai, S. Tamura and N. Imanaka, *Ceram. Int.*, 2023, **49**, 1502–1506.
18 S. Tachibana, C. Zhong, K. Ide, H. Yamasaki, T. Tojigamori, H. Miki, T. Saito, T. Kamiyama, K. Shimoda and Y. Orikasa, *Chem. Mater.*, 2023, **35**, 4235–4242.
19 D. Kato, P. Song, H. Ubukata, H. Taguro, C. Tassel, K. Miyazaki, T. Abe, K. Nakano, K. Hongo, R. Maezono and H. Kageyama, *Angew Chem. Int. Ed. Engl.*, 2023, **62**, e202301416.
20 H. Putz, J. C. Schön and M. Jansen, *J. Appl. Crystallogr.*, 1999, **32**, 864–870.
21 R. Oishi, M. Yonemura, Y. Nishimaki, S. Torii, A. Hoshikawa, T. Ishigaki, T. Morishima, K. Mori and T. Kamiyama, *Nucl. Instrum.*, 2009, **600**, 94–96.
22 R. Oishi-Tomiyasu, M. Yonemura, T. Morishima, A. Hoshikawa, S. Torii, T. Ishigaki and T. Kamiyama, *J. Appl. Crystallogr.*, 2012, **45**, 299–308.
23 H. Chen, L. L. Wong and S. Adams, *Acta Crystallogr., Sect. B: Struct. Sci., Cryst. Eng. Mater.*, 2019, **75**, 18–33.
24 K. Momma and F. Izumi, *J. Appl. Crystallogr.*, 2011, **44**, 1272–1276.
25 B. P. Sobolev and N. L. Tkachenko, *J. Less-Common Met.*, 1982, **85**, 155–170.
26 N. Sorokin and M. Breiter, *Solid State Ionics*, 1997, **99**, 241–250.

 

27 A. Düvel, J. Bednarcik, V. Šepelák and P. Heitjans, *J. Phys. Chem. C*, 2014, **118**, 7117–7129.
28 R. Higashinaka, H. Endo, J. Kajitani, T. D. Matsuda and Y. Aoki, *Phys. B*, 2018, **536**, 824–826.
29 Y. Chi, H. G. Xue and S. P. Guo, *Inorg. Chem.*, 2020, **59**, 1547–1555.
30 W. P. Davey, *Phys. Rev.*, 1922, **19**, 248–251.
31 A. Demourgues, A. Tressaud, H. Laronze and P. Macaudière, *J. Alloys Compd.*, 2001, **323–324**, 223–230.
32 M. Y. Ma, D. Han, N. K. Chen, D. Wang and X. B. Li, *Materials*, 2022, **15**, 7715.
33 H. Ubukata, F. Takeiri, K. Shitara, C. Tassel, T. Saito, T. Kamiyama, T. Broux, A. Kuwabara, G. Kobayashi and H. Kageyama, *Sci. Adv.*, 2021, **7**, eabf7883.
34 K. Mori, A. Mineshige, T. Saito, M. Sugiura, Y. Ishikawa, F. Fujisaki, K. Namba, T. Kamiyama, T. Otomo, T. Abe and T. Fukunaga, *ACS Appl. Energy Mater.*, 2020, **3**, 2873–2880.
35 K. Motohashi, Y. Matsukawa, T. Nakamura, Y. Kimura, N. Kuwata, Y. Uchimoto and K. Amezawa, *Sci. Rep.*, 2022, **12**, 5955.
36 J. G. Bednorz and K. A. Müller, *Z. Phys. B: Condens. Matter*, 1986, **64**, 189–193.